Article Identifier
DOI: 10.22032/dbt.58938
URN: urn:nbn:de:gbv:ilm1-2023isc-093:2

60th ILMENAU SCIENTIFIC COLLOQUIUM
Technische Universität Ilmenau, 4 – 8 September 2023
URN: urn:nbn:de:gbv:ilm1-2023isc:1

IMAGING THE MECHANICAL PROPERTIES OF NANOWIRE ARRAYS

Tianran Ma[a], Michael Fahrbach[a], Jiushuai Xu[a], Frank Eric Boye Anang[a], Maximilian Vergin[a], Florian Meierhofer[a], Uwe Brand[b], Andreas Waag[a], Erwin Peiner[a]

[a]Technische Universität Braunschweig, Institute of Semiconductor Technology (IHT), Hans-Sommer-Straße 66 and Laboratory for Emerging Nanometrology (LENA), Langer Kamp 6a/b, 38106 Braunschweig, Germany
[b]Physikalisch-Technische Bundesanstalt (PTB), Bundesallee 100, 38116 Braunschweig, Germany

ABSTRACT

Dimensional and contact resonance (CR) images of nanowire (NW) arrays are measured using our new-developed CR imaging (CRI) setup. Then a reference method is employed to calculate the indentation modulus of NWs ($M_{i,NW}$) representing the elasticity of NWs, by measuring NW arrays (NWAs) and reference samples at the same static probing force. Furthermore, topography is imaged in combination with CR and $M_{i,NW}$ separately by software, whereby the relation between both parameters of NWAs is visualized. As typical examples, 3D imaging of topography and $M_{i,NW}$ is performed with Si<111> pillar, Cu and ZnO NWAs. The novel method allows for fast mechanical performance measurements of large-scale vertically-aligned NW arrays (NWAs) without releasing them from their substrates.

Index Terms - Nanowire Arrays (NWAs), 3D Contact resonance imaging (CRI), Indentation modulus of NWs ($M_{i,NW}$)

1. INTRODUCTION

Nanowires (NWs)-based nanoelectromechanical systems (NEMS) are attractive for powering autarkic micro-nano systems due to efficient energy-harvesting and storage capability, benefitting from their exceptional optical, electrical, thermal, and mechanical properties [1], [2]. From the viewpoint of fabrication and application, mechanical properties of NWs are crucial factors, which must be considered during the design process. NEMS have the ability to transduce physical effects such as forces into electrical signals. The magnitude of deformation is determined not only by environmental forces but also the NEMS's mechanical properties such as their stiffness. Therefore, over the past decade great research efforts have been made on characterizing mechanical properties of NWs. But due to NW's small physical size, with typical diameters from 10 nm to 500 nm and high aspect ratios from 1 to 300 or even larger than 1000 [3], [4], experimental work has been so far limited to specially prepared individual NWs, e. g., using atomic force microscopy (AFM), in which the tested NWs must be removed from their substrate and fixed on a special one [5]. However, next-generation energy-harvesting (photovoltaics, thermoelectrics, etc.) and storage devices (Li ion battery, super capacitor, etc.) or metal bumps for low-resistance room-temperature fine-pitch bonding on flexible substrates rely on large-scale vertically-aligned NW arrays (NWAs), which have to be characterized without releasing them from their substrates [6], [7]. Our new-developed contact-resonance imaging (CRI) setup based on piezoresistive silicon microcantilever probes (Figures 2 and 3)

© 2023 by Tianran Ma. et al. – Licensee Technische Universität Braunschweig, Deutschland.

This is an Open Access article distributed under the terms of the Creative Commons Attribution ShareAlike-4.0 International License, (https://creativecommons.org/licenses/by-sa/4.0/).

can measure dimensional and mechanical parameters of vertical NWAs at high throughput [8]. Topography and CRI of NWAs are obtained by constant force control loop (FCL) and CR-frequency tracking based on real-time phase-lock-loop (PLL) control, respectively. It is thus different from previous research that was limited to CR testing of individual lying or upright NWs [9], [10]. In addition, a reference method is employed to calculate the indentation modulus of NWs ($M_{i,NW}$) representing the elasticity of NWs. Furthermore, topography is imaged in combination with CR and $M_{i,NW}$ separately by software, whereby the relation between both parameters of NWAs is visualized.

2. NANOWIRE ARRAYS AND CRI SETUP

2.1 Nanowires arrays

The samples used in this study are <111> silicon pillar, copper, and ZnO NWAs, which were fabricated at the Technische Universität Braunschweig, Institute of Semiconductor Technology (TUBS-IHT). According to Figure 1(a), a collection of Si<111> pillar NWs that are (907 ± 12) nm in diameter (D), (614 ± 21) nm in height (H), and (3.422 ± 0.264) µm in pitch (P), where the mean values are given as the arithmetic averages and the uncertainties are given as the standard deviations, have been fabricated by cryogenic deep reactive ion etching (cryo-DRIE) combined with nanoimprint lithography [11]. In comparison with lithographic techniques, the Cu NWAs were produced by a template method, which featured copper deposition in porous polycarbonate membranes [12]. Cu NWAs of irregular dimensions are shown in Figure 1(b), with an exemplary one highlighted that is 173 nm in diameter and 918 nm in height.

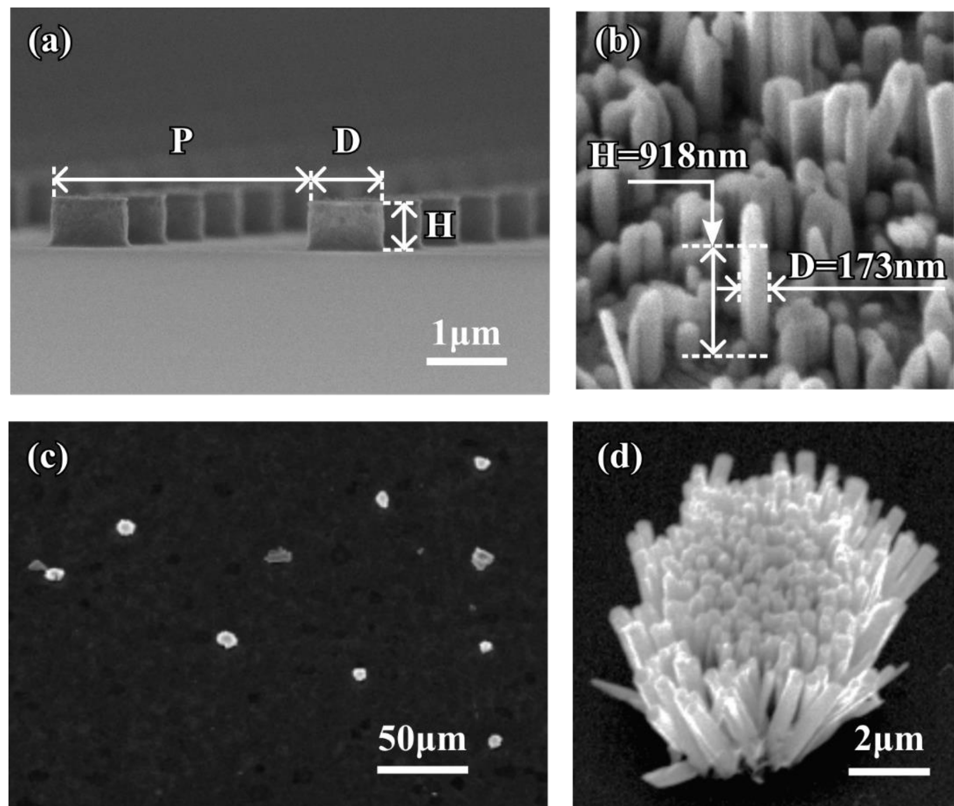

Figure 1. Scanning electron microscopy (SEM) images of (a) silicon pillar, (b) copper and (c), (d) ZnO NWAs.

Finally, bunches of ZnO NWs, which are visible in Figure 1(c) as white dots on a dark background, were area-selectively grown on a Si<100> wafer by chemical bath deposition.

© 2023 by Tianran Ma. et al. – Technische Universität Braunschweig, Deutschland.

Prior to the growth of the ZnO NWs, a Zn nanofilm of ~200 nm in thickness has been sputtered and oxidized in a photolithographically defined area as a seed-layer. For the experimental details, we refer to our reported works [13], [14]. One of the ZnO NW bundles is depicted in an enlarged representation in Figure 1(d).

2.2 CRI setup

For topography and CR imaging, microprobes developed by TUBS-IHT in collaboration with Physikalisch-Technische Bundesanstalt (PTB) and Forschungsinstitut for Microsensorik (CiS) GmbH, Erfurt were used which are based on slender pieoresistive monocrystalline silicon cantilevers [15], [16]. They were purchased from CiS GmbH under the model no. CAN50-2-5. The cantilever is 5 mm long, 200 µm wide, 50 µm thick and has a mass of roughly 0.1 mg, as illustrated in Figure 2 and Table 1. At the free end of the cantilever, an octagonal pyramidal silicon tip with a height of roughly 100 µm is incorporated. The Wheatstone bridge, located near the cantilever's clamping, converts its out-of-plane bending into a voltage output.

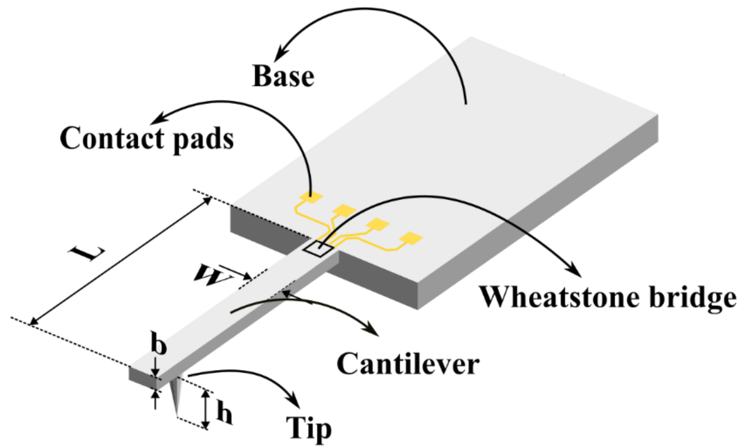

Figure 2. Schematic of piezoresistive cantilever microprobe.

Table 1. Parameters of CAN50-2-5.

Parameter	Symbol	Value
Length	L	5 mm
Thickness	b	50 µm
Width	w	200 µm
Tip height	h	100 µm
Young's modulus	E (Si<100>, cantilever along <110>)	169 GPa

The schematic of the CRI setup [8] developed at TUBS-IHT is shown in Figure 3. The sensor is positioned on an *xyz*-stage with a piezo-actuator at a tilt angle of 15°. While its probing tip is in contact with the surface of a sample and the output DC voltage $\overline{U}_S$ of the Wheatstone bridge reaches a set value, it is actuated out-of-plane by a piezo-actuator (PL055.3x, Physik Instrumente (PI) GmbH & Co. KG). The output signal $U_S(t) = \widehat{U}_S \times \cos(2\pi f t + \varphi_S) + \overline{U}_S$ of the Wheatstone bridge is connected to a Lock-in amplifier (LIA) to extract amplitude $\widehat{U}_S$ and phase φ_S independently. The Wheatstone bridge output signal is analog and converted to digital

© 2023 by Tianran Ma. et al. – Technische Universität Braunschweig, Deutschland.

by analog-to-digital converters (ADC) integrated with microcontroller (ATXMEGA256A3U, Microchip Technology Inc.) and transmitted to an external personal computer (PC). An AGC that changes the actuation amplitude $\hat{U}_A$ keeps the signal amplitude constant. A PLL that sets the actuation frequency f keeps the phase constant. The actuation signal $U_A(t) = \hat{U}_A \times \cos(2\pi f t)$ is created and delivered to the piezo-actuator by a frequency generator (FGEN) based on direct digital synthesis (DDS), digital-to-analog converter (DAC) and a piezo-driver (PZDV). Simultaneously, a FCL is used to maintain the DC-component $\overline{U}_S$ of the Wheatstone bridge's output signal, which is associated with the static probing force, constant by modifying the *xyz*-stage's *z*-position using an external PC. The CR and topography of the NWAs can thus be measured and used for $M_{i,NW}$ determination.

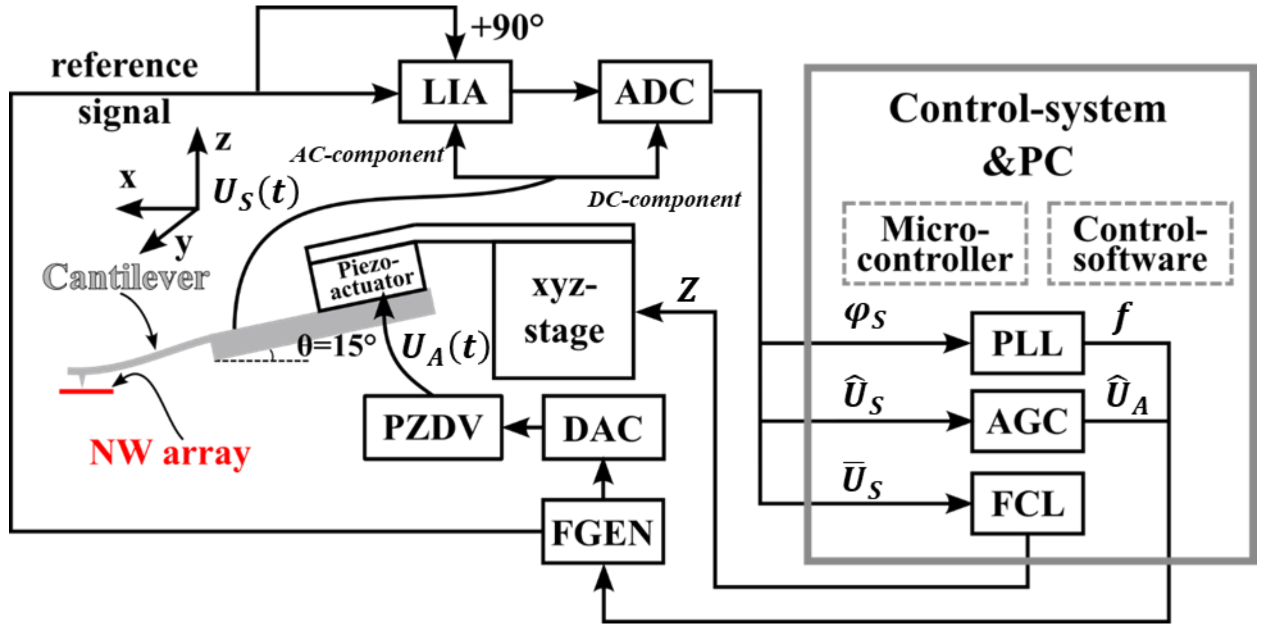

Figure 3. Schematic of the CRI setup.
(The components LIA, ADC, FGEN, DAC, PZDV and Control-system are homemade.)

3. RESULTS AND DISCUSSION

3.1 Free resonance measurement

Figure 4 depicts the free resonance spectrum of the piezoresistive cantilever probe's fundamental resonance mode observed in air. A free resonance frequency of f_0 = 13.791 kHz, which is connected to the vertical stiffness or spring constant (k_{lever}) of the cantilever (Eq. (3.1)), is obtained by fitting a Fano-resonance line shape to the observed magnitude and phase (Fano LSA) [17], [18].

$$k_{lever} = \frac{Eb^3w}{4L^3} \tag{3.1}$$

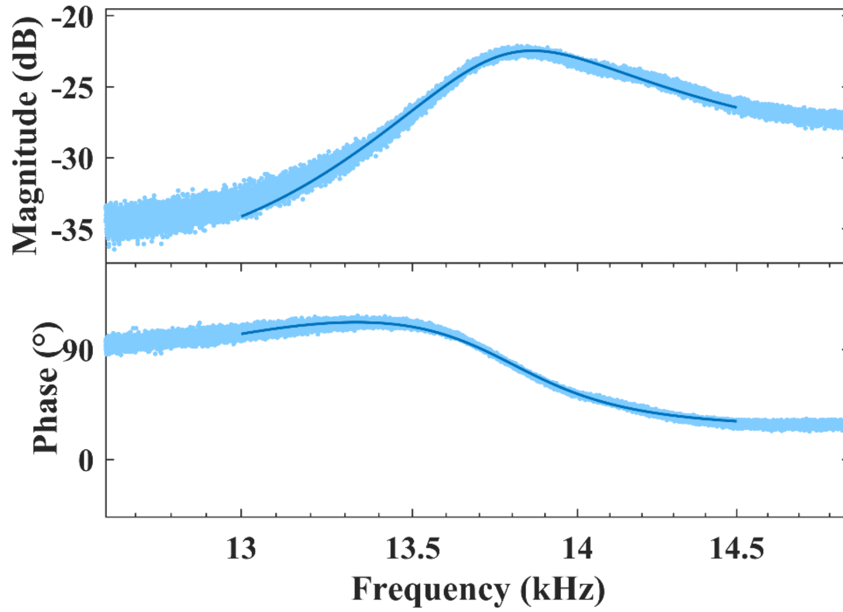

Figure 4. Magnitude and phase vs. frequency around the free resonance mode.

3.2 Contact resonance and indentation modulus measurement

Figure 5 depicts the model for Hertzian contact between a hemispherical tip with radius of curvature (R) and the top surface of a nanowire. When the sensor tip makes contact with the sample, a normal static force (F_N) is subjected in axial direction to NW via the cantilever-tip deflection (Δz) [19]:

$$F_N = k_{lever} \times \Delta z \tag{3.2}$$

Then, on the sample surface, a circular contact with radius of a is established. $M_{i,tip}$ and $M_{i,NW}$ are the indentation moduli of the tip and the NW, respectively.

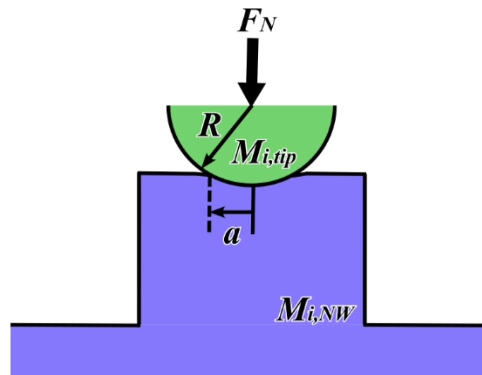

Figure 5. Schematic of Hertzian contact between a hemispherical tip and a NW via its top surface.

The contact stiffness (k_{NW}) is determined by a and the reduced elastic modulus for the tip-NW system (E_{NW}^*) and the above parameters [19].

$$k_{NW} = 2aE_{NW}^* \tag{3.3}$$

© 2023 by Tianran Ma. et al. – Technische Universität Braunschweig, Deutschland.

$$a = \sqrt[3]{\frac{3RF_N}{4E_{NW}^*}} \quad (3.4)$$

$$E_{NW}^* = M_{i,tip} \times M_{i,NW} / (M_{i,tip} + M_{i,NW}) \quad (3.5)$$

The k_{NW} can be estimated using the cantilever stiffness (k_{lever}, Eq. (3.1)) and the resonance frequencies f_0 and f_{NW} measured in air and in contact with the NW independently [10]:

$$k_{NW} = k_{lever} \left[\left(\frac{f_{NW}}{f_0} \right)^2 - 1 \right] \quad (3.6)$$

Theoretically, one could derive experimental values for R and F_N and calculate a using Eqs. (3.6) and (3.3). Then, E_{NW}^* and consequently $M_{i,NW}$ could be determined using Eqs. (3.4) and (3.5). However, because of the micro/nanoscopic size of the tip, it is extremely difficult to correctly determine the parameter R. Additionally, while being in contact with a sample, the silicon tip continuously changes its size and shape due to wear. To circumvent these problems, a reference method was used to measure the indentation modulus of NWs ($M_{i,NW}$). This technique was developed by Rabe and colleagues [20] for measuring the indentation modulus of bulk materials using CR-FM techniques.

During this study, the reference sample (subscript ref) was bulk single crystalline Si<111> with the known indentation modulus (M_i) as listed in Table 2. The measurements were taken on both the NWAs (subtitle NW) and reference samples at the same F_N levels. Then the reduced elastic modulus for the tip-NWAs system (E_{NW}^*) can be displayed as follows:

$$E_{NW}^* = E_{ref}^* \times \left(\frac{k_{NW}}{k_{ref}} \right)^{\frac{3}{2}} = E_{ref}^* \times \left(\frac{\frac{k_{NW}}{k_{lever}}}{\frac{k_{ref}}{k_{lever}}} \right)^{\frac{3}{2}} = E_{ref}^* \times \left[\frac{\left(\frac{f_{NW}}{f_0} \right)^2 - 1}{\left(\frac{f_{ref}}{f_0} \right)^2 - 1} \right]^{\frac{3}{2}} \quad (3.7)$$

The indentation modulus of NWAs ($M_{i,NW}$) can be computed using Equation 3.3 as follows:

$$M_{i,NW} = E_{i,NW}^* \times M_{i,tip} / (M_{i,tip} - E_{NW}^*) \quad (3.8)$$

In this experiment, the indentation modulus of the reference sample ($M_{i,ref}$) and cantilever tip ($M_{i,tip}$) are the theoretical values of the indentation modulus (M_i) of the corresponding bulk material shown in Table 2.

Table 2. Theoretical values of the indentation modulus (M_i) of the reference sample and probing tip, respectively.

Component	Symbol	Material	indentation modulus (M_i/GPa)
Tip	$M_{i,tip}$	Si<100>	165[20]
Reference sample	$M_{i,ref}$	Si<111>	175[20]

Figures 6 (a), (c) independently depict the CR frequency 3D and 2D imaging of silicon pillar NWAs. The CR frequency 2D-top imaging of copper NWAs is shown in Figure 8 (a). The shift

in the resonance frequency of the cantilever from air to contact is caused by the contact stiffness (k_{NW}) between the piezo-resistive cantilever probe and the NWAs.

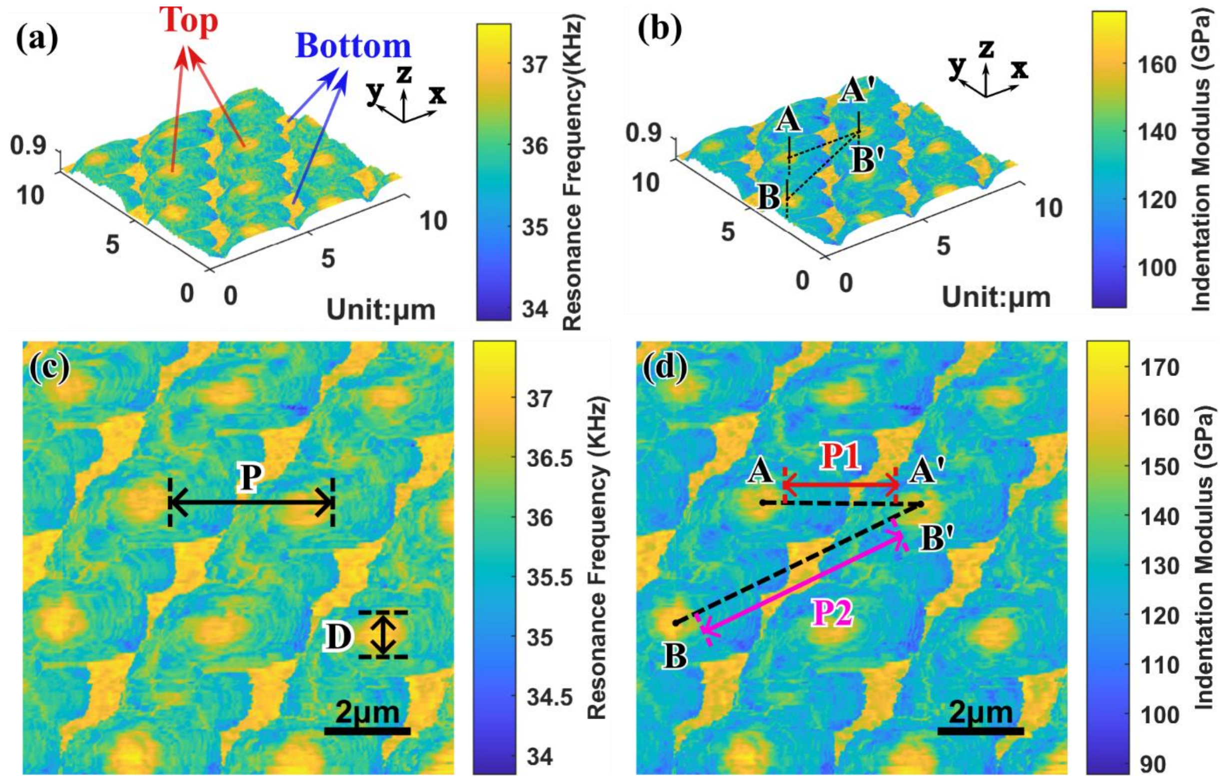

Figure 6. CR frequency (a), (c) and indentation modulus (b), (d) imaging of silicon pillar in 3D (a), (b) and 2D (c), (d) representations (contact force ≈ 7.6 μN).

Table 3. Measured values of Si<111> pillar NWAs' dimensions.

Parameter	Symbol	by SEM	by CRI
Diameter	*D*	(907 ± 12) nm	(865 ± 155) nm
Pitch	*P*	(3.422 ± 0.264) μm	(3.64 ± 0.55) μm
Height	*H*	(614 ± 21) nm	<900 nm

Figure 6 shows 3D as well as 2D-top images of CR frequency (f_{NW}) and indentation modulus ($M_{i,NW}$) of silicon pillar NWAs. The scan speed was adjusted to a minimum of 1 μm/s with 201 lines in order to provide high-resolution findings. The z values indicate the topography of the NWAs and the color bars show either the NWAs' f_{NW} as determined by the CRI setup or $M_{i,NW}$ which is calculated using f_{NW}. The mechanical properties are combined with the topography by software. The highest f_{NW} and $M_{i,NW}$ are both found on the top surface of the silicon pillar NWs and between the NWs. The most likely explanation is that the contact state changes in the course of the scan. The tip has a cone-like shape, which touches the top surface of the NW with its apex, as seen in Figure 5. However, the tip makes contact with the NWs by the side of the cone when it moves away from the top surface of the NWs, as illustrated in Figure 7(a). Then, as shown in Figure 7(b), the cone's apex comes again into touch with the silicon bottom, but only if the space between consecutive NWs is large enough.

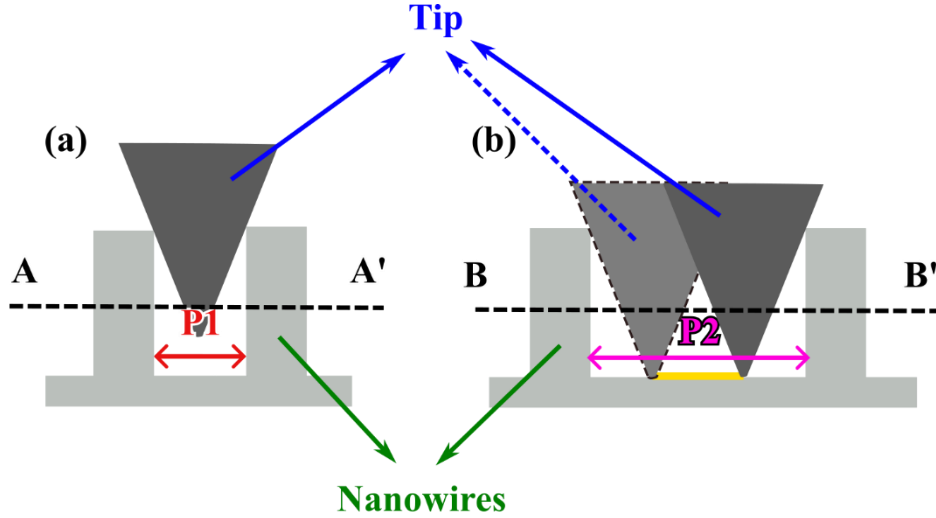

Figure 7. Schematic of cross-sections of sensor's tip and NWs during scanning.

In this approach, single NWs can be clearly distinguished, and the diameter (*D*), pitch (*P*), and height (*H*) of the Si<111> pillar NWs can then be determined by analyzing the considered f_{NW} image as shown in Figure 6(a), (c). Table 3 compares the measured dimensional NWA values that were obtained using SEM and CRI, respectively. Meanwhile, Figures 6(b), (d) show the $M_{i,NW}$ values estimated from the f_{NW}, with the greatest $M_{i,NW}$ centered near the center of the top surface of the NWs, slightly higher than at the edge. The ranges of experimental values are compared with the theoretical values of bulk material in Table 4, revealing that the measured $M_{i,NW}$ at the center of the NWs' top surface are near the theoretical values.

Table 4. Measured indentation modulus values ($M_{i,NW}$) at the NWs' top-surface vs. theoretical values (M_i) of bulk material.

Sample	by Theory (M_i/GPa)	by CRI ($M_{i,NW}$/GPa)	Deviation
Si<111> NWs	$M_{Si<111>}$ = 175 [20]	175 — 150	~ (-14.3% — +0%)
Copper NWs (Unknown crystal phase)	$M_{Cu<100>}$ = 129 [21]	120 —160	~ (-7.5% — +24.1%)
	$M_{Cu<110>}$ = 138 [21]		~ (-13.1% — +15.9%)
	$M_{Cu<111>}$ = 141 [21]		~ (-14.9% — +14.2%)

For the copper NWAs, the scan speed was also set to 1 µm/s with 101 lines for high-resolution conditions. The diameter of a NW protruding from the rest was measured by SEM to be approx. 173 nm in Figure 1 (b), which agrees with the value of approx. 169 nm estimated by CRI in Figure 8 (a) of the corresponding wire. The examined $M_{i,NW}$ of the Cu (unknown crystal phase) nanowire shown in Figure 8 (b) compared with the theoretical value of bulk material is also presented in Table 4, which follows the same behavior of Si<111> pillar NWs with the largest $M_{i,NW}$ appearing in the center of the NW's top-surface while decreasing towards the edges.

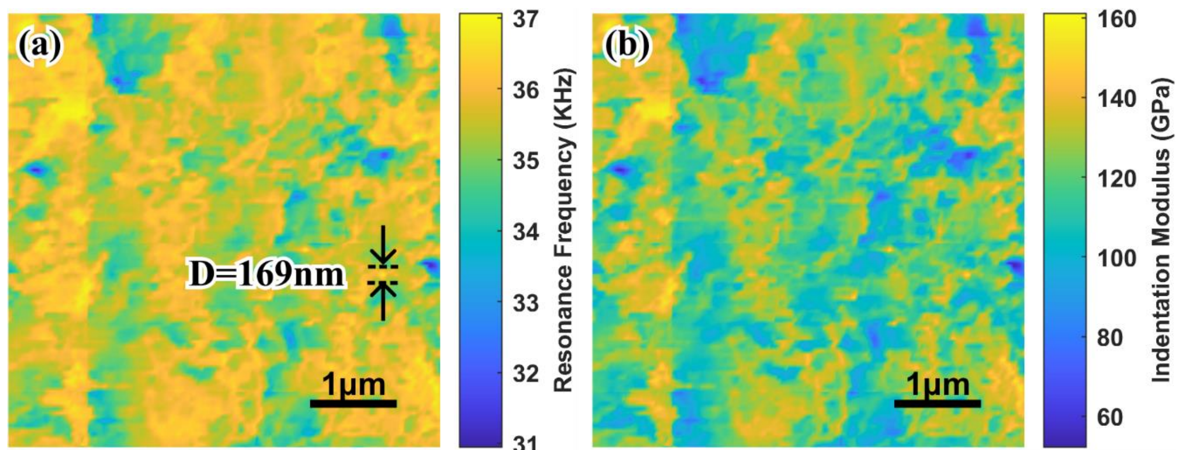

Figure 8. CR frequency (a) and indentation modulus (b) 2D imaging of copper NWs (contact force ≈ 7.6 μN).

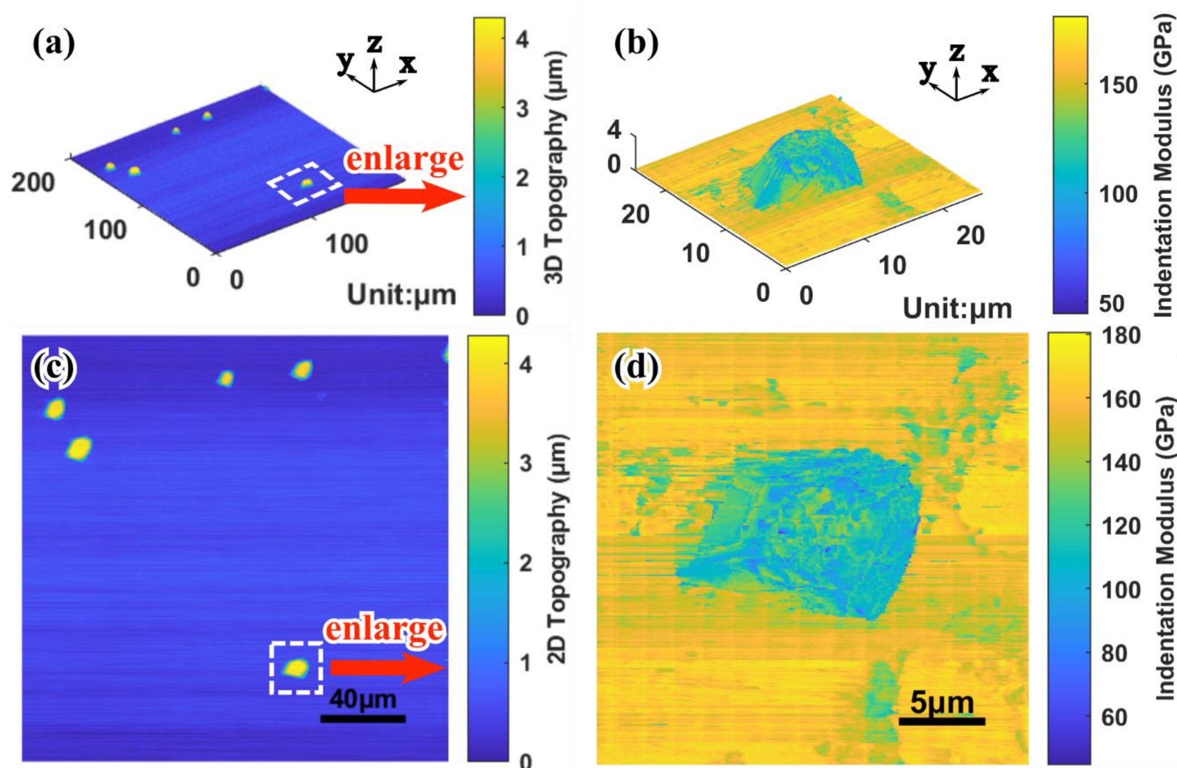

Figure 9. Topography (a), (c) and indentation modulus (b), (d) imaging of ZnO NWAs in 3D (a), (b) and 2D (c), (d) representations (contact force ≈ 7.6 μN).

Figure 9 (a) and (c) show the 3D and 2D topography images, respectively, of bundles of ZnO NWAs within a sample area of 200 μm × 200 μm. To speed up the process, here, resolution was decreased to 501 lines with a scanning speed of 100 μm/s. The yellow areas in the topography image with a height of roughly 4 μm corresponds to ZnO NWA bundles. For the dashed white marked section of 25 μm × 25 μm, CR imaging was performed at a decreased scanning speed of 1 μm/s at 501 lines in order to obtain the indentation modulus image of a single ZnO NWA bundle. The outcome is displayed in Figures 9 (b) and (d) in 3D and 2D representation, respectively. As shown in Figure 10, the observed $M_{i,NW}$ values of ZnO NWAs as showed in Figure 9 (d) are displayed in a histogram, exhibiting a convolution of two Gaussian peaks [22], which are fitted to obtain mean $M_{i,NW}$ values and matching material of the two regions. Table

5 compares the experimental results, where the uncertainties are given as the full width at half maximum of the Gaussian distributions, with theoretical values for Si<100> and ZnO<0001>. According to the reasonable matching of theory and experiment, and a comparison of indentation modulus image with topography, the green/blue area indicate the ZnO NWA bundle, and the orange/yellow represents the Si<100> substrate in Figures 9 (b), (d).

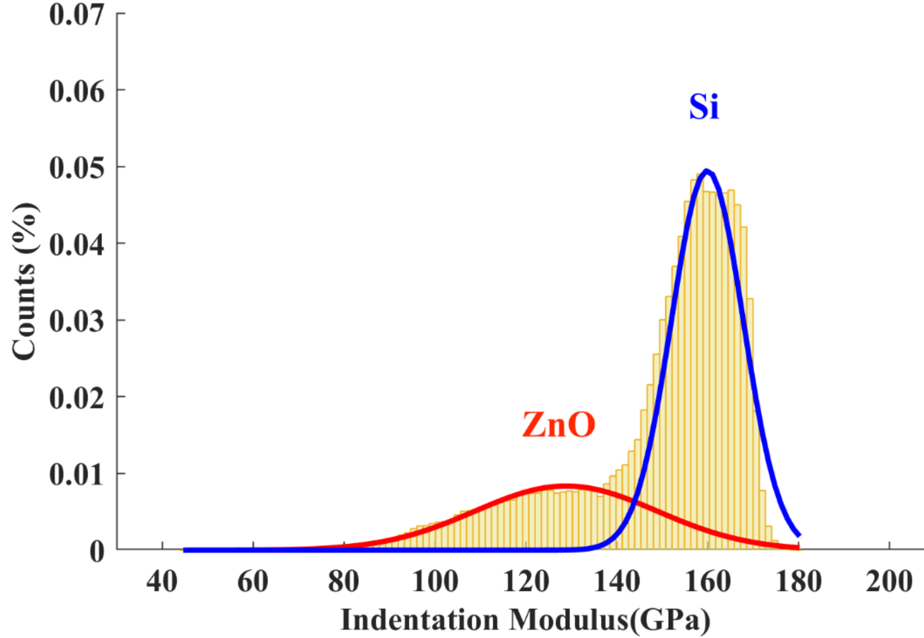

Figure 10. Histogram of the measured indentation moduli in Figure 9 (d).

Table 5. Measured values of indentation modulus ($M_{i,NW}$) at ZnO NWA on Si<100> vs. theoretical values (M_i) of bulk material.

Material	by Theory (M_i/GPa)	by CRI ($M_{i,NW}$/GPa)	Deviation
Si<100> substrate	$M_{Si<100>}$ =165 [21]	(159.99±18.59)	~(- 14.3% — +8.2%)
ZnO NWs (Unknown crystal phase)	$M_{ZnO<0001>}$ = 143^b	(128.91±47.39)	~(- 42.3% — +23.3%)

[b] The theoretical values were calculated from the elastic stiffness constants of single-crystalline ZnO<0001> (c_{11} = 207 GPa, c_{12} = 117.7 GPa, c_{13} = 117.7 GPa, c_{33} = 209.5 GPa, c_{55} = 44.8 GPa, c_{66} = 44.6 GPa) [23] by explicit approximations of elasticity orthotropic solids for conical indenters [24].

4. CONCLUSION

In this study, we used a newly developed CRI setup and software to accomplish 3D imaging of topography, CR frequency, and $M_{i,NW}$ on Si<111> pillar, copper, and ZnO nanowire arrays (NWAs) without releasing them from their substrates. Dimensional parameters determined by CRI for the Si<111> pillar and copper NWAs agree reasonably well with the values investigated by scanning electron microscopy (SEM). Meanwhile, the largest $M_{i,NW}$ values emerged in the center of the NW's top-surface and decreased towards the edges. The measured differences between NWs' ($M_{i,NW}$) and bulk's theoretical indentation modulus (M_i) values

correspond to the well-known size effect in NWs' elastic behavior and may be attributed to surface stress [25]. Topography and indentation modulus imaging of ZnO NW bundles was shown to help in detecting their position on the silicon wafer as well as their identification via characteristic distributions related to ZnO and silicon in an indentation modulus histogram.

5. ACKNOWLEDGEMENT

This research project is supported by the European Union and is funded within the scope of the European Metrology Programme for Innovation and Research (EMPIR) project 19ENG05 NanoWires entitled 'High throughput metrology for nanowire energy harvesting devices' (https://www.ptb.de/empir2020/%20nanowires/home/).

REFERENCES

[1] S. Raman, A. Ravi Sankar, and M. Sindhuja, "Advances in silicon nanowire applications in energy generation, storage, sensing, and electronics: a review," *Nanotechnology*, vol. 34, no. 18, p. 182001, 2023.
[2] S. Mokkapati and C. Jagadish (Eds.), *Nanowires for energy applications*. Academic Press, 2018.
[3] C. J. Murphy and N. R. Jana, "Controlling the Aspect Ratio of Inorganic Nanorods and Nanowires," *Adv. Mater.*, vol. 14, no. 1, pp. 80–82, 2002.
[4] J. Kim, J. Cui, and K. A. Fichthorn, "Solution-Phase Growth of Cu Nanowires with Aspect Ratios Greater Than 1000: Multiscale Theory," *Acs Nano*, vol. 15, no. 11, pp. 18279–18288, 2021.
[5] A. G. N. Sofiah, M. Samykano, K. Kadirgama, R. V. Mohan, and N. A. C. Lah, "Metallic nanowires: Mechanical properties – Theory and experiment," *Appl Mater Today*, vol. 11, pp. 320–337, 2018.
[6] M. Wlazło *et al.*, "Piezoelectric Response and Substrate Effect of ZnO Nanowires for Mechanical Energy Harvesting in Internet-of-Things Applications," *Materials*, vol. 15, no. 19, p. 6767, 2022.
[7] A. P. Nugroho *et al.*, "Vertically Aligned n-Type Silicon Nanowire Array as a Free-Standing Anode for Lithium-Ion Batteries," *Nanomaterials-basel*, vol. 11, no. 11, p. 3137, 2021.
[8] M. Fahrbach *et al.*, "Contact Resonance Imaging with Vertical Nanowire Arrays," Nuremberg, Germany: VDE, May 2022.
[9] S. Wang, Z. Shan, and H. Huang, "The Mechanical Properties of Nanowires," *Adv Sci*, vol. 4, no. 4, p. 1600332, 2017.
[10] M. F. Fatahilah *et al.*, "Traceable Nanomechanical Metrology of GaN Micropillar Array," *Adv Eng Mater*, vol. 20, no. 10, p. 1800353, 2018.
[11] G. Hamdana *et al.*, "Nanoindentation of crystalline silicon pillars fabricated by soft UV nanoimprint lithography and cryogenic deep reactive ion etching," *Sensors Actuators A Phys.*, vol. 283, pp. 65–78, 2018.
[12] M. E. T. Molares *et al.*, "Etched heavy ion tracks in polycarbonate as template for copper nanowires," *Nucl Instruments Methods Phys Res Sect B Beam Interactions Mater Atoms*, vol. 185, no. 1–4, pp. 192–197, 2001.
[13] J. Xu *et al.*, "Area-Selective Growth of Aligned ZnO Nanorod Arrays for MEMS Device Applications," *Proceedings*, vol. 2, no. 13, p. 887, 2018.
[14] J. Xu *et al.*, "Fabrication of ZnO nanorods and Chitosan@ZnO nanorods on MEMS piezoresistive self-actuating silicon microcantilever for humidity sensing," *Sensors Actuators B Chem.*, vol. 273, pp. 276–287, 2018.

© 2023 by Tianran Ma. et al. – Technische Universität Braunschweig, Deutschland.

[15] E. Peiner, M. Balke, L. Doering, and U. Brand, "Tactile probes for dimensional metrology with microcomponents at nanometre resolution," *Meas Sci Technol*, vol. 19, no. 6, p. 064001, 2008.
[16] U. Brand *et al.*, "Long Slender Piezo-Resistive Silicon Microprobes for Fast Measurements of Roughness and Mechanical Properties inside Micro-Holes with Diameters below 100 µm," *Sensors*, vol. 19, no. 6, p. 1410, 2019.
[17] M. Fahrbach *et al.*, "Damped silicon microprobes for high-speed roughness measurements," presented at the MikroSystemTechnik Congress 2021, Stuttgart-Ludwigsburg, Germany: VDE, Nov. 2021.
[18] A. Setiono *et al.*, "Performance of an Electrothermal MEMS Cantilever Resonator with Fano-Resonance Annoyance under Cigarette Smoke Exposure," *Sensors Basel Switz*, vol. 21, no. 12, p. 4088, 2021.
[19] D. C. Hurley, "Contact resonance force microscopy techniques for nanomechanical measurements," *Nanosci Technol*, pp. 97–138, 2009.
[20] U. Rabe *et al.*, "Imaging and measurement of local mechanical material properties by atomic force acoustic microscopy," *Surf Interface Anal*, vol. 33, no. 2, pp. 65–70, 2002.
[21] J. J. Vlassak and W. D. Nix, "Measuring the elastic properties of anisotropic materials by means of indentation experiments," *J Mech Phys Solids*, vol. 42, no. 8, pp. 1223–1245, 1994.
[22] G. Stan and W. Price, "Quantitative measurements of indentation moduli by atomic force acoustic microscopy using a dual reference method," *Rev Sci Instrum*, vol. 77, no. 10, p. 103707, 2006.
[23] I. B. Kobiakov, "Elastic, piezoelectric and dielectric properties of ZnO and CdS single crystals in a wide range of temperatures," *Solid State Commun*, vol. 35, no. 3, pp. 305–310, 1980.
[24] A. Delafargue and F.-J. Ulm, "Explicit approximations of the indentation modulus of elastically orthotropic solids for conical indenters," *Int J Solids Struct*, vol. 41, no. 26, pp. 7351–7360, 2004.
[25] M. N. Esfahani and B. E. Alaca, "A Review on Size-Dependent Mechanical Properties of Nanowires," *Adv Eng Mater*, vol. 21, no. 8, p. 1900192, 2019.

CONTACTS

Tianran Ma, M. Sc — email: tianran.ma@tu-braunschweig.de
ORCID: https://orcid.org/0009-0009-6884-7439

Prof. Dr. Erwin Peiner — email: e.peiner@tu-braunschweig.de
ORCID: https://orcid.org/0000-0001-5801-813X

Maximilian Vergin, M. Sc — email: m.vergin@tu-braunschweig.de
ORCID: https://orcid.org/0009-0006-3319-1714

Dr. Florian Meierhofer — email: f.meierhofer@tu-braunschweig.de
ORCID: https://orcid.org/0000-0002-5578-7731

Prof. Dr. Andreas Waag — email: a.waag@tu-braunschweig.de
ORCID: https://orcid.org/0000-0002-2724-1686

© 2023 by Tianran Ma. et al. – Technische Universität Braunschweig, Deutschland.